Materials Advances

ROYAL SOCIETY OF CHEMISTRY

PAPER

View Article Online
View Journal | View Issue

Cite this: *Mater. Adv.*, 2025, **6**, 6764

Hierarchical magnetic self-assembly of few-nanometer rutile TiO_2 particles *via* magnetron sputtering

Jarkko Etula,[a] Camilla Tossi,[b]†* Niklas Wester,[a] Daryna Ihnatiuk,[b] Sami Sainio,[c] Kai Arstila,[d] Timo Sajavaara,[d] Ilkka Tittonen[b] and Jari Koskinen[a]

Few nanometer-sized rutile TiO_2 nanoparticles were synthesized at room temperature, using conventional reactive magnetron sputtering gas aggregation, with a large permanent magnet placed under the deposition substrate. The presence of the magnet caused the rutile TiO_2 nanoparticles to self-assemble into a branching, hierarchical particle agglomerate structure, with a large surface area comprising various pore sizes. These structural features appear to be due to ferromagnetism induced by surface oxygen vacancies in anatase and rutile TiO_2, or to electrostatic charging effects. The resulting chain-like structures present themselves as a film 10 micrometers in thickness. As observed by helium ion microscopy, and scanning as well as transmission electron microscopy, this structure is highly porous featuring remarkably high specific surface areas, quantified as 650 m^2 g^{-1} by BET nitrogen absorption measurement. The elemental composition, chemical bonding, and purity of the collected rutile TiO_2 nanoparticles were analyzed by TOF-ERDA, XAS, and TEM EDS, as well as FTIR, UV-Vis, and Raman spectroscopies, confirming the prevalence of the rutile phase. This highly porous and easily accessible structure was able to photocatalytically degrade dyes at rates compatible with the typical photocatalytic performance of rutile TiO_2. We believe that upon further development, this synthesis technique holds great potential for the selective synthesis of high-purity few-nanometer-sized rutile without the need for high temperatures, providing a facile fabrication route for a reference model system in photocatalytic conversion reactions.

Received 28th February 2025,
Accepted 19th August 2025

DOI: 10.1039/d5ma00186b

rsc.li/materials-advances

1 Introduction

For the last 50 years, titanium dioxide has repeatedly been demonstrated to be a remarkable material in terms of photocatalytic and photoelectrochemical applications.[1–3] The uses of interest for TiO_2 range from photoelectrochemical water splitting, to pollutant degradation both in liquid and in gaseous media, as well as to cosmetic use in sunscreens.[4,5] Additionally, the relative ease of fabricating TiO_2 thin films and nanoparticles, low cost, chemical and thermal stability, Earth abundance, ease of modification, and low toxicity concur to classifying it as an attractive material in all of its phases.[6,7] Notably, it is possible to tailor the crystal phase, the doping level, and the surface states to a level that allows versatility in the destined application.[8,9] Temperature stability of TiO_2 crystal phases may however be problematic depending on the application, as all TiO_2 crystal phases are irreversibly converted to rutile between 700 and 920 °C.[10] Rutile phase is hence the most stable TiO_2 crystal phase, and it is usually synthesized by high-temperature methods.[11] Advantages of rutile over other TiO_2 phases are the higher melting point, which makes it appropriate for catalytic applications where a high temperature is needed, and stability against turning into other phases. Additionally, oxygen vacancies on the surface of rutile and anatase TiO_2 can enhance photocatalytic performance,[12,13] and they also exhibit ferromagnetism,[14–16] which are both of importance in the present study.

Photocatalysis is of great importance for the removal of pollutants at an industrial level, through processes that not only contribute to environmental remediation, but achieve so through the exploitation of no other energy source than sunlight: one of the main uses of photocatalysis is the decomposition of organic molecules such as dyes, which are diffuse pollutants, inefficient to degrade solely by chemical means. In

[a] *Department of Chemistry and Materials Science, Aalto University, Kemistintie 1, Espoo, Finland*
[b] *Department of Electronics and Nanoengineering, Aalto University, Tietotie 3, Espoo, Finland. E-mail: camilla.tossi@zarm.uni-bremen.de*
[c] *Department of Electrical Engineering and Automation, Aalto University, Otaniementie 17, Espoo, Finland*
[d] *Department of Physics, University of Jyväskylä, 40500 Jyväskylä, Finland*
† Present address: ZARM, University of Bremen, Germany.

spite of the degradation difficulty, the decomposition of dyes is a simple method for the assessment of the potential use of a material as a photocatalyst.[17] More complex methods can yield accurate information, for example the decomposition of acetic acid, through the evaluation of the production of gas byproducts.[18,19] Metal oxides are commonly used to enable widespread utilization of photocatalysis, since they are inexpensive, non-toxic, and Earth-abundant, all while retaining the structural and morphological properties optimal for photocatalytic performance,[20–22] with TiO_2 nanoparticles being a versatile and performing photocatalyst for pollutant removal.[23,24] The ideal materials for photocatalysis have both maximal surface area and volume compared to mass, meaning that a single light source, for example the sun, would be able to illuminate a large volume both in terms of depth and total surface area. One possible structure would consist of such small nanoparticles that are on the lower size limit of stability. This would offer (i) very high surface area per mass, (ii) minimal losses from reflection, and (iii) scattering from round small particles, to facilitate effective illumination at greater material depths. Common problems with such small particles are agglomeration and packing of particle films, grain size growth, and subsequent loss of surface area and porosity that decrease their performance as photocatalysts. Ideally, a hierarchically porous outward-branching fractal structure would be able to resolve these issues by providing structural support, a large surface area, and a high absorption rate for backscattered photons. An additional advantage is that the variety of pore sizes can support catalytic activity both in liquid media (where smaller pores help the capillary diffusion of the liquid) and in gaseous media (where large pores increase the dry gas diffusivity).[25,26]

Gas aggregation is commonly used as a method for particle synthesis. One embodiment of this, for example, is the use of a conventional magnetron sputter or hollow cathode operated at sufficiently high gas pressures in vacuum to decrease the temperature of produced species, to induce particle nucleation, after which the particles can be collected.[27,28] This allows physical vapor deposition (PVD) methods, which are usually limited to the fabrication of 2D films, to create very porous high surface area films consisting of nanoparticles.[26,29] Such films can however become denser if constructed from very small nanoparticles. TiO_2 films and nanoparticles fabricated by magnetron sputtering have demonstrated to be especially suitable for photocatalysis and other light-responsive applications.[7,11,28] Recently, Ekeroth *et al.*[30–32] have described and demonstrated the collection of magnetic nanoparticles from a hollow cathode source using permanent magnets. In their work, ferromagnetic nickel-oxide and iron nanoparticles self-assembled along the field lines of the magnet into remarkably long chains, 50 μm long, demonstrating high porosity. In the current work, we demonstrate a similar magnetic collection of TiO_2 nanoparticles, synthesized from a conventional direct-current magnetron sputter operated at higher chamber pressures in reactive oxygen-starved Argon atmosphere. Few-nanometer-sized ($\sim$3 nm) TiO_2 nanoparticles have been previously deposited for example by Ahadi *et al.*[27] in a dedicated magnetron cluster aggregation source. Room-temperature ferromagnetism of rutile and anatase TiO_2 nanoparticles has been widely studied and is attributed to oxygen vacancies.[14–16] The prevalence of these oxygen vacancies has been located commonly onto the surfaces of thin films and nanoparticles.[33,34] Hence, it is expected that the relative force a magnetic nanoparticle experiences in the magnetic field would increase as the particle size decreases. This type of ferromagnetism has been measured to be 4 times higher in rutile, when compared to anatase.[14]

Hence, titanium dioxide nanoparticles were synthesized in a reactive oxygen-starved deposition environment using an unmodified Kurt J. Lesker AXXIS toroidal direct current (DC) magnetron sputter with a Ti target, using parameters similar to the work by Ahadi *et al.*[27] In the present study, a 70 mm diameter Nd-based disc magnet is placed under the substrates that collect the synthesized nanoparticles. The S pole of the magnet is oriented axially towards the center N pole of the magnetron, unbalancing the conventional field in the magnetron sputter. After 30 minutes deposition at 150 W power, a 10 μm thick layer of TiO_2 particles is collected radially in a ring-shape on the substrate. As investigated by electron and helium ion microscopy methods, the resulting structure is an open, branching, hierarchical particle agglomerate structure comprising both various sizes of openings and closings. In addition to demonstrating the applicability of the high surface area and porosity of this structure in photocatalysis, the spectral characteristics were thoroughly investigated by UV-visual, Infrared, and Raman spectroscopies. The elemental purity and composition of the structure was revealed in fine detail by time-of-flight elastic recoil detection analysis (TOF-ERDA) and X-ray absorption spectroscopy (XAS). Field cooled (FC) magnetization tests were also performed for the collected samples, to investigate the residual magnetization of the final product. This investigation resulted in the room-temperature synthesis of highly pure rutile nanoparticles, assembled in a hierarchical and fractal-like structure, which demonstrated photocatalytic activity comparable with more complex fabrication methods.

2 Experimental

Synthesis

Titanium dioxide nanoparticles were synthesized in an oxygen starved deposition environment using a 2 inch toroidal unmodified Kurt J. Lesker AXXIS magnetron sputter, using parameters similar to the work by Ahadi *et al.*[27]

A large cylindrical axially magnetized permanent NdFeB magnet of 70 mm in diameter and 35 mm in thickness (1.35 T residual magnetism, N45) was placed 8 cm away from the surface of a 99.995% purity 2 inch titanium sputter target, as depicted in Fig. 1(a). An aluminum foil was placed onto the magnet, as a collecting subsrate. Similarly to literature,[27] the reactive sputtering atmosphere was 90 sccm of argon and 0.7 sccm oxygen resulting in 385 mTorr of pressure, as controlled by an Edwards XDS 10 dry scroll pump. After 30 minutes at 150 W power (280–290 V, 510–520 mA) a 10 m thick layer of

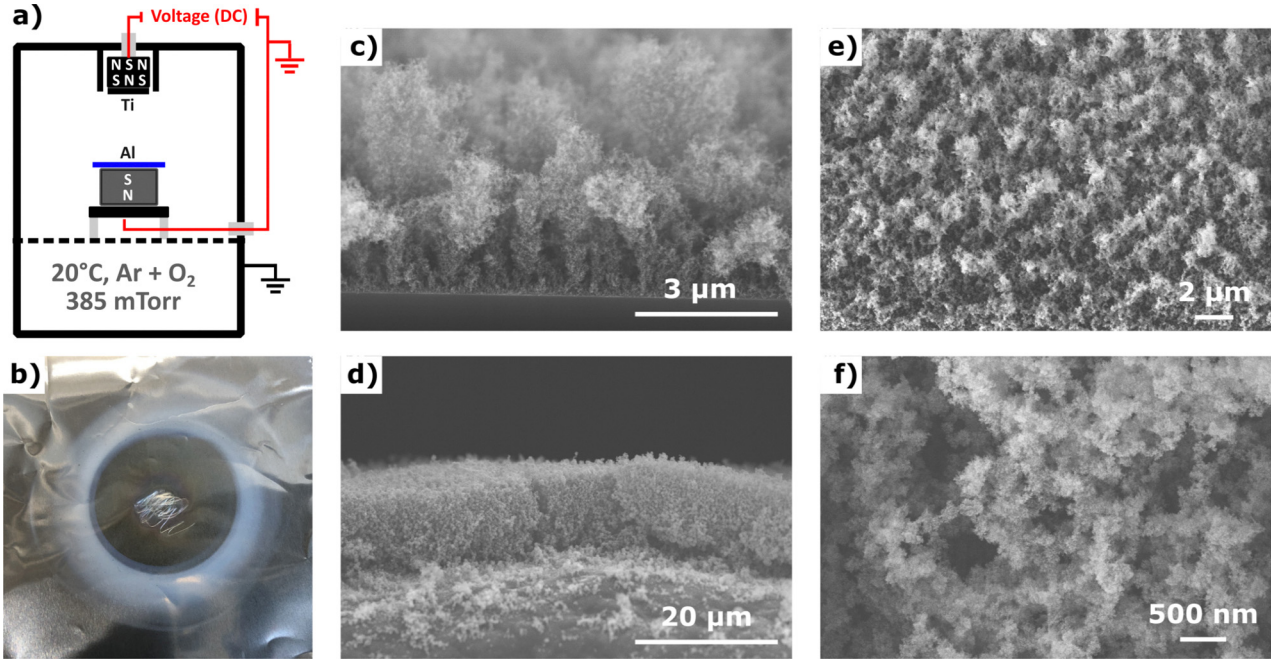

Fig. 1 On the left, (a) conventional direct current magnetron sputtering vacuum setup, with a 2″ titanium target (in gray) at 80 mm working distance. Aluminum foil substrate (in blue) is placed onto a 70 mm diameter permanent magnet. (b) Photograph of aluminum foil after deposition, showing the radial deposition of titanium dioxide nanoparticles. The inner strong white radial pattern is 40 mm in diameter, whereas the outer white streaks are 70 mm, as corresponding to the diameter of the magnet under the substrate. The center of the foil was fixed to the substrate holder by double-sided copper tape to make a good electrical contact. At the center (c) and (d), scanning electron microscopy (SEM) images of a cross-section of the deposited particle-structure, as deposited on a on Si wafer (c), and on Al foil (d). On the right (e) and (f), helium ion microscopy (HIM) images of a cross-section of the sample shown in (d), showing the high porosity and depth of the structure.

particles was found collected radially in a ring-shape. The system was pumped to a base pressure of 1×10^{-6} Torr using a CTI cryogenics CTI 8F cryopump.

The gas aggregation nanoparticle formation in an oxygen-deficient atmosphere is known to favor the formation of sub-stoichiometric rutile clusters that become fully oxidized when exposed to ambient air.[35] The deposition parameters were selected *a posteriori* for the synthesis of nanoparticles of few nm in size, achieving a thickness and accumulation of particles sufficient for characterization.

The substrate was electrically grounded and the electrical current passing from substrate to ground was measured to be around −480 mA, which is about 93% of the total current supplied by the magnetron DC power source. Hence, the function of anode during the deposition is absolved by the deposition substrate instead of the underlying substrate holder. If the substrate grounding was removed, the measured open-circuit floating potential between substrate and ground was measured to be around −12 V.

Mass weighing

The weight of the TiO_2 particles was measured by a Mettler Toledo XP2U, with a repeatability of 0.25 μg and a readability of 0.1 μg. Experimental error was determined to be around 0.5 μg by repeating the measurement process for multiple readings. Particles were released from the Al-foil substrate into vials filled with 2-propanol (>99.95%, 1 ppm evaporation residue, Sigma-Aldrich) by sonication at 44 kHz. The mass change of the Al-foil with TiO_2 particles was measured after evacuation to 3 mTorr under turbo pump to remove adsorbed moisture and solvent. This procedure was repeated at 10–20 second sonication intervals, to see the total mass lost due to particles being removed. Blank Al-foil substrate was also checked to evaluate possible loss of Al-foil mass during sonication and sample handling.

Morphological and chemical characterization

Cross-sectional scanning electron microscopy (SEM) analysis of the samples was performed with a Hitachi S-4700 SEM equipped with a field emission electron source, operated at 15 kV accelerating voltage. Cross-sectional samples were prepared from silicon samples by cleaving, and from Al and Cu foils by cutting with scissors. Surface morphology was further studied with a Zeiss Orion Nanofab helium-ion microscope (HIM) at the Nanoscience Center of the University of Jyväskylä. TEM and TEM EDS analysis were performed by a JEOL JEM-2800 operated at 200 kV. Sample were prepared onto M75 copper-only TEM grids (Agar) and densified by acetone drop.

Visible-Raman spectroscopy was performed on a Horiba Jobin-Yvon Labram HR confocal Raman system, with a 488 nm argon laser, 10 mW power on the sample, and an Olympus 100× objective. Raman spectra were acquired in the range of 50 to 1000 cm^{-1} with a 600 lines per inch diffraction grating, exposure time of 15 s, and accumulation averaging

count of two. Spectroscopic calibration was performed on intrinsic Si wafer (Ultrasil). UV-Vis reflectance spectra of the TiO_2 nanoparticles were measured *via* a Flame-S UV-vis spectrometer by Ocean Optics, using a halogen lamp as light source, and an integration sphere for collecting the signal. The acquired spectra were normalized against the bare aluminum substrate. Attenuated total reflection Fourier transform infrared (ATR FTIR) spectroscopy measurements were carried out using a Bruker FTIR ALPHA II spectrometer with a platinum ATR sampling module (diamond) in the spectral range of 400–4000 cm^{-1}. Elemental depth profiles were measured using a time-of-flight recoil detection analysis system (TOF-ERDA). A detailed description of the method and apparatus can be found in literature;[36] the ion beam was a 15.315 MeV 127I8+ from the 1.7 MV Pelletron accelerator at the Accelerator Laboratory of the University of Jyväskylä. The tilt angle was 20 degrees relative to the ion beam direction. The acquired data was analyzed using Potku software.[37]

Soft X-ray XAS experiments were conducted at the Stanford Synchrotron Radiation Lightsource (SSRL) beamline 8-2, where a bending magnet was used with a 55° incidence angle (magic angle) to the X-ray beam. A resolution of ~200 meV was achieved with a spherical grating monochromator which was operated using 40 × 40 μm slits. The X-ray beam spot size was approximately 1 × 1 mm^2 with a total flux of 1010 photons per s. The X-ray energy was scanned from 260 to 350 eV, 380 eV to 440, 450 to 490 and 520 to 580 eV for carbon 1s, nitrogen 1s, titanium 2p edges, and oxygen 1s respectively. Each edge was acquired from three different locations. A Keithley picoammeter was used for amplifying the drain current, to collect all the data in total electron yield (TEY) mode, where the incoming flux was measured using a nickel grid coated with Au sputtered film. Here, a reference sample was used for energy calibration of the data prior to the data analysis. The C 1s spectra were confirmed to match their energy calibration by observing the sp^2 π^* and carboxyl functionalities.[38] The N 1s spectra were energy corrected and aligned using Ni 2p signal in 2nd order at 426.35 eV. The Ni 2p is available *via* a reference sample inserted upstream, which cuts about 2% of the incoming intensity. The O 1s spectra were first aligned by matching their oxygen i_0 dip (roughly at 530 eV) and then further aligned to match the carbon tape O 1s π^* to 532.0 eV. Finally, all the data were background-subtracted and energy-corrected using IGOR Pro v. 8.02 software.

The specific surface area of both the TiO_2 sample and its aluminum foil substrate were measured at 77.35 K using nitrogen adsorption isotherm performed with a BELsorp-mini II instrument (BEL, Japan) equipped with a dead volume cell. The Brunauer, Emmett, and Teller (BET) method was used to calculate the surface area of the samples, tested over a relative pressure range of 0.05 to 0.45 on the adsorption isotherm. All calculations were performed using the BELMaster (BEL, Japan) analysis software (version 6.4.1.0). Field cooled (FC) magnetization was measured from 1.8 to 300 K by Quantum Design PPMS DynaCool Physical Property Measurement System with a resolution of 0.016 mT, equipped with a 9 T magnet and cryogen-free temperature control.

Photocatalytic dye degradation

The dyes used in the present study are Rhodamine 6G (R6G) and Methylene Blue (MB), purchased from Sigma-Aldrich. The dyes were diluted in de-ionized water at a concentration of 10 μM for Rhodamine 6G and 30 μM for methylene blue, and the samples were immersed in the solutions for 60 minutes in the dark, to reach adsorption–desorption equilibrium between the dyes and the photocatalyst. Afterwards, they were illuminated for 120 minutes at a light intensity of 25 mW cm^{-2}, equivalent to 0.25 suns, by a sun simulator HAL-320W, manufactured by Asahi. During the experiment, the dye concentration in solution was maintained uniform by magnetic stirring. The aluminum foil was cut into samples of 1 cm^2, with deposited rutile particles on it, and were were glued to a cuvette, since other methods of particle collection and distribution to the experimental vessel did not prove effective. The decomposition of the dye was observed by acquiring the transmittivity of the solution with an UV-vis spectrometer (Ocean Optics HR2000) and by using Beer–Lambert's law as a model for the decreasing dye concentration in the aqueous medium. The transmittivity was computed at wavelengths corresponding to the maximum absorption of each dye (525 nm for R6G and 664 nm for MB). Blank experiments in dark and under irradiation were performed, to exclude the possible input of other components of the system to the dye degradation efficiency of the studied material.

3 Results and discussion

Scanning-electron microscopy (SEM) images in Fig. 1 show initial deposition tests, where TiO_2 nanoparticles were collected onto a silicon wafer using the permanent magnet placed under the substrate. The Si wafer substrate was later changed to Al and Cu foils, due to their higher relative permittivity of about 1. The branching fractal structure in Fig. 1(c) begins as several smaller branches close to the substrate, but only a small number of branches grows taller and widens away from the substrate. Fig. 1(d) shows a thicker TiO_2 structure collected onto an aluminum foil during a longer 30 minute collection. Note the absence of any dense thin film, *i.e.* the structure appears to consist only of particle aggregates. The high porosity and openness of the TiO_2 structures is comparable with structures deposited by Ekeroth *et al.*,[30,32] who collected ferromagnetic Ni/NiO and Fe particles into distinct chains. In their work, however, the permanent magnet with the substrate was placed further away, and off-axis from the gas aggregation source, while in the current work the magnet is placed directly under the substrate, to maximize collection efficiency, on-axis with the DC-MS source as shown in Fig. 1(a).

To further validate the present concept of on-axis magnetic collection, TiO_2 nanoparticles were also collected on copper foils and silicon wafers, and ferromagnetic Fe/FeO_x nanoparticles sputtered from an iron target were also collected onto copper foil, as shown in Fig. S1 in the SI. The corresponding particle structure as imaged by SEM is detailed in Fig. S2 in the SI.

Fig. S2 shows a nanoparticle chain structure closely resembling the long self-assembled chains also observed by Ekeroth *et al.*[30,32] in their off-axis magnetic collection. This seems to validate the viability of on-axis magnetic collection of not only the ferromagnetic Fe/FeO_x nanoparticles, but also the TiO_2 particles discussed in the present work: since the TiO_2 particles in Fig. 1 collect into a similar radial ring pattern as also observed for Fe/FeO_x particles in Fig. S1 and S2, we take this as an indication that the TiO_2 particles should also be similarly magnetic.

TiO_2 nanoparticle ferromagnetism due to surface oxygen vacancies in oxygen-starved environments is widely discussed in literature.[14,39,40] These presumed magnetic properties of the deposited TiO_2 branching structure were investigated *ex situ* in field cooling magnetism (FC) measurements, as shown in Fig. S3 in SI, but no significant ferromagnetism was observed when compared to the magnetic behavior of blank Al foil. Literature on similarly synthesized TiO_2 nanoparticles,[27,35] suggests that any exposure to the atmosphere is found to rapidly further oxidize the surfaces of the few nanometer-sized TiO_2 nanoparticles, thus suppressing the surface oxygen vacancies and causing the loss of the ferromagnetic behavior that allowed the formation of hierarchical nanostructures.

It should be noted that in both of the on-axis magnetic collections (TiO_2 and Fe/FeO_x) the center part of the substrate is free from any large particle structures (Fig. 1(b) and Fig. S1). It is expected that electrons originating from magnetron would follow field lines, and hence concentrate on the center of the magnet due to their low mass/charge ratio. Fig. S4 in SI shows a picture taken during the Fe/FeO_x nanoparticle collection at longer working distances of 22 cm, where the visually illuminated plasma originating from the magnetron sputter appears to be confined to the center of the substrate and the permanent magnet placed underneath. Electrostatic charging effects should be hence considered when depositing such small nanoparticles, especially when depositing electrically resistive films and structures using DC magnetron sputtering. Recent work[41] has demonstrated the unusual formation of micrometer-sized well-separated Li_xTiO_2 pillars during conventional perpendicular DC sputtering under −5 V substrate self-bias and 60 mTorr Ar pressure. In that study, the substrate self-biasing was achieved by adjusting the resistance of grounding, *i.e.* impeding the substrate from discharging. Therefore, similar effects could also be observed in the current work, where an oxide nanoparticle structure is deposited onto an electrically grounded substrate under oxygen starved reactive sputtering conditions.

Hence, it can be difficult to distinguish if the self-assembly mechanism of this branched structure shown in Fig. 1 is solely due to the *in situ* ferromagnetic properties of TiO_2 particles, or if other forces such as electrostatic interactions between charged particles and substrate also play a significant role. Nevertheless, this geometrical effect induced by the magnetic field from the disc magnet placed under the substrate resulted in particles depositing in a radial ring pattern on the substrate, as shown in Fig. 1(b). It is also possible that the high flux of electrons and charged species incident on the center increase the rate of etching and desorption, overcoming the deposition rate. Additional microscopical and characterization efforts were carried out, to better understand the structure and properties of this deposited ring pattern.

The 10 um thick nanoparticle structure was also investigated using Helium-ion microscopy (HIM), as shown in Fig. 1(e) and (f). Compared to SEM, the high depth-of-field imaging capabilities of HIM allow a better visualization of the internal porosity and depth of the openings in the TiO_2 particle structure. In Fig. 1(f) a hierarchical structure consisting of different sizes of opening and closings is observed: particle aggregates measuring few micrometers across appear to consist of smaller aggregates that are hundreds of nanometers in diameter. These can be further broken down into aggregates tens of nanometers in size, and finally only a few nanometers in size, as further explored by transmission electron microscopy (TEM) in Fig. 2(a) and (b). The crystallinity of the deposited structure is also investigated using select area electron diffraction (SAED) in Fig. 2(c), obtaining a diffraction pattern characteristic to rutile TiO_2[42] (COD pattern 96-901-5663). A SAED pattern collected from a larger area is also radially integrated and plotted with annotated diffraction peaks in Fig. S5 and S6 in SI.

The SAED pattern in Fig. 2 shows visible reflections only corresponding to the rutile TiO_2 structure. This is surprising, considering that the formation of for example anatase and brookite TiO_2 is also possible, as found by other studies done on reactive titanium sputtering processes in oxygen environments.[27,43] Nonetheless, SAED is not accounting for

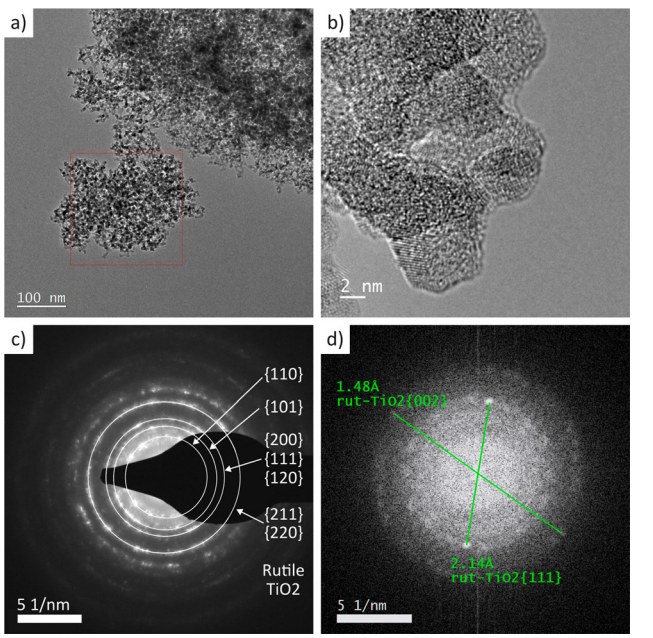

Fig. 2 (a) TEM micrograph of the deposited TiO_2 nanoparticles, and (b) high-resolution TEM micrographs showing the small nanocrystals, 3–5 nm in size. (c) SAED from the area noted by red box in (a): the electron diffraction rings are annotated to rutile TiO_2 (COD 96-900-4142). (d) FFT of the micrograph shown in (b), showing multiple crystalline *d*-spacing, corresponding to rutile TiO_2 families of planes.

possibly amorphous nanoparticles. The synthesis and magnetic collection described in the current work appears to either selectively produce rutile TiO_2 particles, or to filter or repel other synthesized particles from the observed collection area, for example by magnetic and electrostatic effects.

High-resolution TEM micrographs in Fig. 2 show the highly aggregated structure consisting of smallest crystalline features in the range of 2–5 nm in size, but it can be difficult to visually separate overlapping smaller particles from the larger features approximately 5 nm in size. The existence of amorphous features cannot be ruled out either. The elemental composition as investigated by TOF-ERDA in Table 1 indicates relatively high amounts of carbon (13 at%) present in the structure, which may coat and hide the outer edges of the few nanometer sized TiO_2 particles. Nevertheless, the crystalline planes visible in Fig. 2(b) indicate crystallite size in the 2–3 nm size range. A fast Fourier transform (FFT) from the TEM micrograph in the inset shows crystalline planes belonging to the rutile TiO_2 structure, as in agreement with Fig. 2(c). It should be noted that the local heating effects of the electron beam in TEM can accelerate particle coalescence and result in larger particle and crystallite size. This should be however unlikely for particles 2–3 nm in diameter, that have a melting point commonly reported somewhere between 1000–2200 K.[44,45]

Electron microscopy revealed a highly porous structure consisting of few-nanometer sized nanoparticles. Nitrogen adsorption and BET analysis were carried out to allow for a more quantitative measure of the surface area, and are shown in Fig. 3(a) and Fig. S7. The mass of the particles deposited on the 1 cm^2 area analyzed in BET was measured to be 137 $\mu g\ cm^{-2}$ using an ultra microbalance. The specific surface area (SSA) calculated from the BET analysis indicated an SSA of 650 $m^2\ g^{-1}$ for this TiO_2 nanoparticle aggregate structure. The SSA of uncoated aluminum foil substrate was also measured for reference in BET (SSA 0.307 $m^2\ g^{-1}$, Fig. S7 in SI), and was subtracted from the calculation of SSA for TiO_2 particles.

Assuming the rutile TiO_2 nanoparticles are modeled as smooth spheres that are not in contact with each other, the specific surface area of 650 $m^2\ g^{-1}$ for rutile TiO_2 crystals would correspond to 2.2 nm diameter spherical nanoparticles (assuming density of 4.23 $g\ cm^{-3}$). This suggested nanoparticle size of 2.2 nm is in reasonable agreement with microscopy results, but smaller than the apparent particle size observed in TEM. However, such small porous features can be difficult to observe in TEM from the overlapping particle aggregates shown in Fig. 2. Furthermore, some of the larger particles observed in Fig. 2 may be further porous themselves, or have high surface roughness. Elemental purity of the structure was also investigated qualitatively by scanning transmission electron microscopy energy dispersive X-ray spectroscopy (STEM EDS), and results are shown in SI (Fig. S8) to be consistent with TiO_2 stoichiometry.

The described PVD method allows the synthesis and selective collection of few-nanometer sized rutile TiO_2 particles at room temperature. This result is important since the high temperatures required for rutile formation (between 700 and 920 °C[10]) can also accelerate nanoparticle size growth and structural coarsening. In gas aggregation from a PVD source, control over the chamber gas pressure enables rapid cooling of the forming particles *via* collisions with cool gas, impeding further crystallite growth. This does not however prevent nanoparticles from attaching to each other to form larger clusters, as it was observed in this work.

3.1 Time-of-flight elastic recoil detection analysis (TOF-ERDA)

Elemental purity of the formed TiO_2 structure was investigated quantitavitely using Time-of-Flight Elastic Recoil Detection Analysis (TOF-ERDA). The elemental depth profiles and histograms provided in Fig. S9 and S10 in SI show that all elements are well spread throughout the thickness of the nanoparticle film structure. The TOF-ERDA elemental composition (at%) is provided in Table 1, as computed from the area noted by dashed lines in Fig. S10.

As tabulated in Table 1, there is a high quantity of hydrogen present in the structure, which may be for example in the form of water or surface TiO_2 hydroxyl and functional groups, since the amount of oxygen is also higher than the stoichiometry of TiO_2. This is noteworthy, since the sample remained evacuated at 1×10^8 Torr pressure in the TOF-ERDA measurement chamber, and can be taken as a confirmation of the high structural porosity. High levels of carbon and some nitrogen are also observed, which are expected since porous rutile TiO_2 is a prominent photocatalyst in both carbon dioxide and nitrogen fixation reactions.[46,47] To gain deeper understanding of the elemental composition and purity, the structure was further investigated by Raman spectroscopy, attenuated total reflection Fourier transform infrared spectroscopy (ATR-FTIR), and X-ray absorption spectroscopy (XAS).

Table 1 TOF-ERDA elemental composition (at%) calculated from the area noted by dashed lines in Fig. S10 in SI

Sample	O	H	Ti	C	N	Al
TiO_2	42 ± 2	25 ± 2	17 ± 1	13 ± 1	1.1 ± 0.1	1.3 ± 0.1

3.2 Raman spectroscopy

Raman spectroscopy, carried out at a laser wavelength of 514 nm, is shown in Fig. 3(b) and displays a rutile structure similar to what is typically observed in literature, with peak widths consistent for few nanometer sized rutile TiO_2 particles.[6,48] Carbon impurities, as found by TOF-ERDA, were also more closely investigated with Raman spectroscopy at 633 nm excitation wavelength, as shown in Fig. S11 (SI). However, no significant Raman activity typical to carbon–carbon bonding was found,[49] which may indicate for example surface adsorbed molecular functional groups. This was subsequently further investigated by ATR-FTIR, as shown in Fig. S12 (SI), and by X-ray absorption spectroscopy (XAS) in the following section.

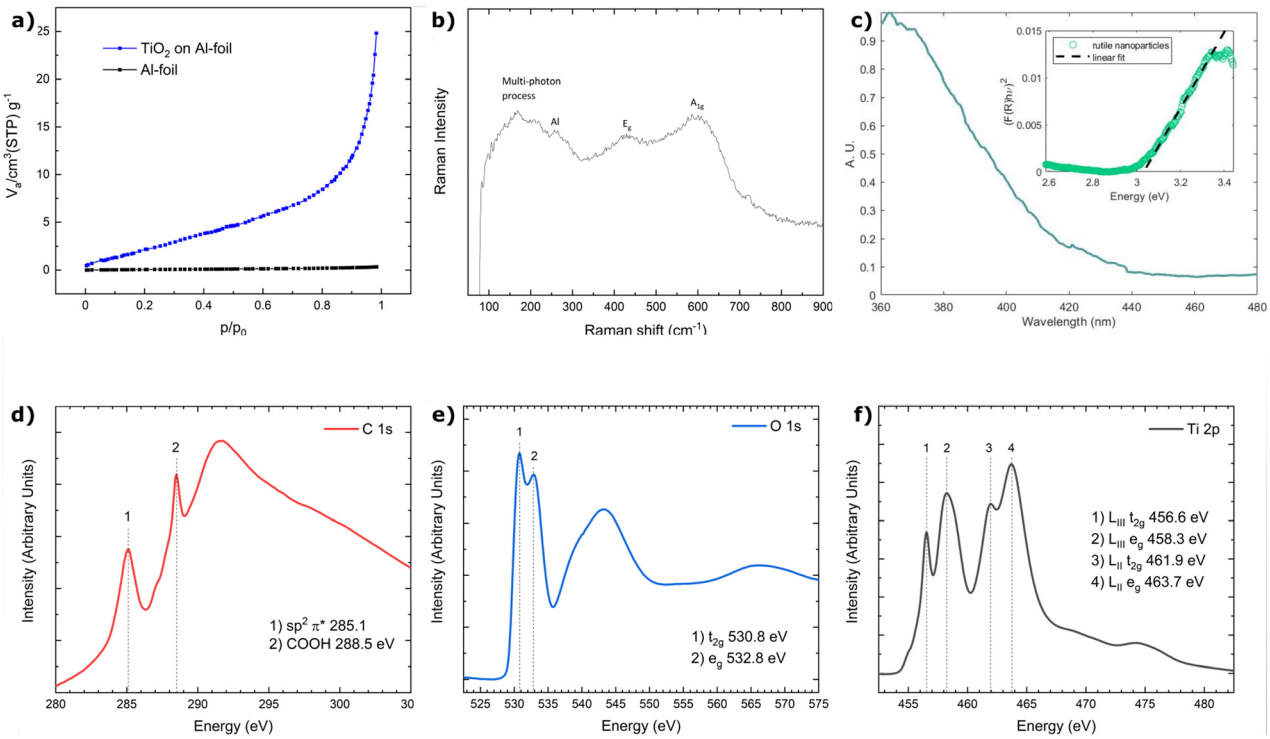

Fig. 3 (a) Nitrogen adsorption isotherm curves collected from 1 cm^2 sample area, consisting of 0.137 mg of TiO_2 nanoparticles deposited onto 7.398 mg of Al foil. BET-plot of the sample (Fig. S7 in SI), yields a specific surface area (SSA) of 650 m^2 g^{-1} for the TiO_2 nanoparticles. Reference Al foil SSA 0.307 m^2 g^{-1} BET results in Fig. S7. (b) Raman spectra showing prominent but broad rutile features E_g and A_g^1, as well as a comparably very sharp peak originating from the substrate aluminum foil. The peaks originating from TiO_2 are very broad which is in agreement with typical Raman interpretation where increased peak broadening is observed for small rutile TiO_2 nanoparticles.[48] (c) UV-vis spectrum of a rutile nanoparticle layer on Al foil, normalized to eliminate the reflection from the foil. In the inset, Tauc plot of the Kubelka–Munk function, with a linear fit showing an estimated bandgap of 3.03 eV. In the bottom row, absolute intensity X-ray absorption (XAS) spectra in total electron yield (TEY) mode with labeled peaks for (d) C 1s, (e) O 1s, and (f) Ti 2p spectra. See Fig. S13 in the SI for the N 1s spectrum.

3.3 XAS

Following the detection of carbon, titanium, oxygen and nitrogen by TOF-ERDA, C 1s, O 1s, Ti 2p and N 1s spectra were acquired with XAS, as shown in Fig. 3(d–f). Despite the presence of 1.1 at% nitrogen, further analysis of the N 1s spectra is not feasible due to very low intensity observed in the N 1s spectrum (Fig. S13 in SI). The XAS C 1s spectrum shows prominent peaks at around 285.1 eV and 288.5 eV attributed to unoccupied π* states and carboxylic acid groups, respectively.[38] In addition, a broad peak starting at around 292 eV corresponding to sp^2 σ states was observed. Spectral features due to presence of aldehyde (286.1 eV), ketone (286.7 eV), C–H (287.5 eV) and C–OH (289.5 eV) may be present, but are not well resolved due to convolution. The presence of carbonyl functionalities is further supported by several bands in the FTIR spectrum ranging from 1600 to 1713 cm^{-1} in Fig. S12 (SI). Despite the apparent presence of sp^2 hybridized carbon, the absence of the characteristic sp^2 long range order peak at 291.7 eV indicates absence of crystalline graphitic carbon with long range order. Moreover, no D and G bands were observed in the Raman spectra acquired in the range of 1000 to 2700 cm^{-1} (Fig. S11, SI).[49] Hence, the sp^2 hybridized C 1s XAS peaks are not due to the presence of amorphous carbon; it is instead likely that the carbonaceous impurities are present as surface contamination, consisting mainly of small molecules with oxygen containing functionalities, present throughout the thickness of the highly porous TiO_2 films, as also evidenced by the TOF-ERDA analysis (see Table 1 and Fig. S9), possibly from spontaneous photoreduction reactions occurring on the TiO_2 surface.[46,47]

Based on the C 1s spectra, a carboxyl peak is expected in the O 1s spectrum at 532.8 eV,[38] together with peaks for ketone and aldehyde at 530.5 and 531.5, respectively. These peaks are, however, heavily convoluted with the TiO_2 O 1s T_g^2 and E_g peaks. TOF-ERDA showed an 8 at% excess of oxygen: assuming stoichiometric TiO_2, most of the oxygen is expected to be bound to Ti, but excess oxygen, likely bound to carbon, is expected to convolute the O 1s spectrum, making reliable peak assignment difficult. Despite this, the spectral features of the O 1s spectrum and Ti 2p closely resemble those reported for titanium oxides.[50–54] Moreover, the Ti 2p spectrum shows the characteristic two douplet peaks, which are further split into T_g^2 and E_g orbitals in the octahedral symmetry. This peak splitting occurs in titanium oxides, including TiO_2, Ti_2O_3 and TiO, that have an octahedral or a distorted octahedral coordination of oxygen.[51]

The spectral features in both O 1s and Ti 2p are sensitive to phase changes in TiO_2,[52–54] as well as to the oxidation state of

titanium.[51] Sputter-induced reduction of TiO_2 has been reported to cause spectral broadening, red-shifts of the Ti 2p absorption peaks, and a decrease in the energy difference between E_g and T_g^2 peaks in the O 1s spectrum.[51,54] On the other hand, Kucheyev *et al.*[53] reported similar spectra for amorphous TiO_2 and TiO_2 aerogel. Thus, the 2 eV energy difference between E_g and T_g^2 peaks in the O 1s spectrum, visible in Fig. 3(e) could indicate either a lower degree of oxidation than expected TiO_2, or the presence of amorphous TiO_2. This is further supported by the relatively low energy of L_{III} T_g^2 peak of 456.6 eV in the Ti 2p spectrum, in Fig. 3(f). In general, distinguishing the phase of TiO_2 in XAS total electron yield spectra is complicated by formation of surface layers.[51,55] TEM imaging revealed particle sizes of 2–5 nm, and electron diffraction showed possible presence of nanocrystalline rutile. Due to the small particle size of the titanium dioxide nanoparticles, the film is expected to consist of a large number of surface sites. Moreover, the TOF-ERDA analysis depth profile revealed a relatively constant oxygen content thoughout the film. Chen *et al.*[55] reported that small TiO_2 nanoparticles (19 Å) display distortions in the surface Ti sites from octahedral geometry due to truncation of the neighbouring Ti and O atoms caused by the large curvature of such small particles. Interestingly, they also found that the distortions in the surface sites could improve activity in binding functional groups and catalytic activity. Thus, the titanium dioxide nanoparticle film of this work is expected to consist of a large number of surface sites, whose distorted geometry causes the observed broad features on the O 1s and Ti 2p spectra. As rutile and anatase have very similar short-range titanium and oxygen environments, spectral differences have been attributed to long range order.[51,54,56] For all TiO_2 polymorphs, the E_g-related peak is expected to further split into two clearly resolvable peaks.[52,53] Both amorphization and decrease in particle size can be expected to result in loss of long range order resulting in the observed broad of spectral features.[53,55,57] While the overall spectra closely resembles those reported for amorphous or substoichiomtric titanium dioxide, it is also possible that the film consists of a mixture of crystalline and amorphous particles or crystalline TiO_2 nanoparticles with a large number of distorted surface sites.

3.4 UV-visibile light spectroscopy

The absorption spectrum of the sample is obtained from reflectance using the Kubelka–Munk equation, $F(R) = (1 - R)2/2R$). The resulting Kubelka–Munk function is used in lieu of absorbance in a Tauc plot, in order to calculate the bandgap from a linear fit.[58] The spectral acquisition was taken as reflectance from the particles attached to the growth substrate due to their small amount, which prevented the full acquisition and computation of reflection, transmission and absorption spectra from a solution, which is the standard practice. The data suggest a band gap of 3 eV, which is on the narrow side in comparison with typical TiO_2 anatase and rutile bandgaps in nanoparticles,[59] but compatible with bandgap measurements of rutile nanocrystals by photoacoustic spectroscopy[60] and compatible with the optical properties of rutile TiO_2 thin films grown by RF magnetron sputtering.[61] A likely explanation is that the larger assemblies of small nanoparticles, which are evident in the hierarchical structure, are dominating the light scattering, similarly to Mie scattering.[62]

3.5 Photocatalysis

The TiO_2 nanoparticles were investigated for photocatalytic activity: normally, rutile exhibits lower activity than the anatase phase, due to higher surface energy on the active facets of anatase, which allows adsorption and degradation of molecules.[63] However, fabricating rutile nanostructures with high surface areas and with complex hierarchical structures has demonstrated to increase the number of active sites and to promote light absorption, thus improving the photocatalytic activity of the phase.[64] Zhang *et al.*[65] further demonstrated that the normalization of photocatalytic efficiency with respect to the active area shows that rutile and brookite phases perform better than anatase. The rutile TiO_2 nanoparticles fabricated in the present work have demonstrated viable photocatalytic activity on the degradation of two dyes, Methylene Blue (MB) and Rhodamine 6G (R6G). Photocatalytic dye degradation has been long-investigated both as a model of photocatalytic efficiency and as a direct application, since the industrial release of commercial dyes in waste-waters is known to have adverse effects on the health of humans, animals and sea plants. The degradation of MB and R6G are possible thanks to the formation superoxide ions at the semiconductor–solution interface, which in turn cause the formation of hydroxyl radicals, which decompose the dye molecules through various oxidation pathways.[66,67] Rutile is especially prone to the generation of reactive oxygen species,[68,69] moreso if the material is oxidized,[17] as is assumed by the observed lack of ferromagnetism.

The decomposition of the dye on synthesized TiO_2 nanoparticles was observed by taking aliquotes of the dye solution and observing their optical transmissivity *via* a UV-vis spectrometer (Ocean Optics HR2000), using Beer–Lambert's law as a model for the dye concentration in the aqueous medium, and the kinetic coefficient was calculated from the degradation data presented in Fig. 4. Two series of seven samples, produced in seven fabrication rounds with the same recipe, were examined and are identified in the Figure by serial numbers. Fig. 4(a) and (b) show the degradation on the three most efficient samples for each dye, and their comparison to the blank test, which was a sample of the aluminum substrate without any deposited nanoparticle. During the initial period of dye adsorption in the dark, fluctuations are observed in the dye concentration, likely due to adsorption and desorption on the surface of the nanoparticles and on the substrate, before stabilization. In case of Methylene Blue, higher degradation rates were observed in tests with TiO_2 nanoparticles than in blank tests, while in the case of Rhodamine 6G, clear degradation observed in tests with nanoparticles and no photolysis took place on the blank sample. Fig. 4(c) shows the apparent rate constants for all tested samples, tested for each dyes. Taking into account very low load of rutile nanoparticles in conducted experiments,

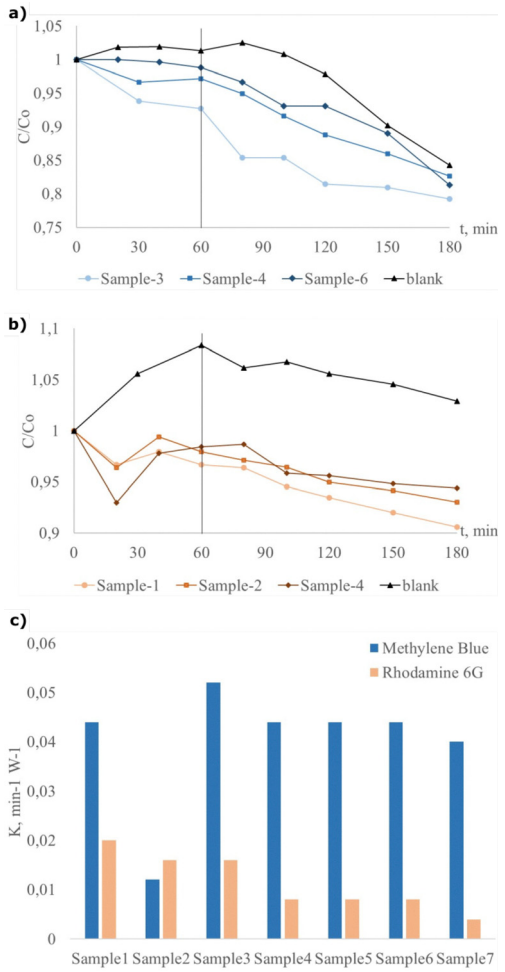

Fig. 4 Dye degradation plots of TiO_2 nanoparticles deposited onto aluminum foil: (a) degradation of methylene blue and (b) degradation of rhodamine 6G of selected samples grown with the same fabrication recipe, in comparison with a blank sample of bare aluminum. (c) Dye degradation rate constants for selected samples from the same fabrication series.

samples have shown photocatalytic behavior compared to those mentioned in literature.

The normalized mass of the photocatalyst present on the aluminum foil has been weighed as 137 μg cm^{-2} for the sample marked as number 6. Considering that the cuvettes used for the degradation were filled with 4 mL of dye solution, the catalyst load was 0.034 mg mL^{-1}. Comparison with the kinetic coefficients with respect to the catalyst load presented in existing literature shows that the catalytic activity is compatible with previous investigation of rutile nanoparticles, supporting the claim that the fabricated rutile nanoparticle structures are a viable candidate for efficient photocatalysis.[21,70–72]

4 Conclusions

Here we have demonstrated how the simple placement of a large permanent magnet under the substrate can be used to modify a typical DC-MS gas aggregation nanoparticle synthesis, enabling the magnetic collection of few-nanometer-sized TiO_2 nanoparticles into highly porous hierarchial self-assembled structures. The resulting hierarchical structure is an open, branching, particle agglomerate structure comprising both various sizes of openings and closings in both nanometer and micrometer scale. The specific surface area of this structure was measured to be 650 m^2 g^{-1} in BET measurement, which is in agreement with the thorough characterization and microscopy efforts. Furthermore, the crystallinity of the few nanometer sized nanoparticles appears to be completely composed of rutile TiO_2, which may be attributed to the higher surface ferromagnetism of rutile nanoparticles, when compared to anatase. The photocatalytic dye-degradation study shows that the synthesized material is viable as a photocatalyst, although further investigation may be worth pursuing with reductive or oxidative reactions that involve transparent media or gas phases. The use of the dry PVD gas aggregation method also allows for the synthesis of high purity nanoparticles in the few-nanometer size scale, as thoroughly characterized here using several different techniques. Since the synthesis of few-nanometer sized rutile TiO_2 nanoparticles is commonly only available *via* wet synthesis methods, this dry room temperature synthesis method offers an alternative to deposit directly onto preferred substrates without risking contamination from wet methods. Such advantages are useful for example when used as model systems, and when depositing on pristine or sensitive surfaces.

Conflicts of interest

There are no conflicts to declare.

Data availability

The experimental data sets and the original micrographs that support the findings of this study are available upon request. These data are stored both by the authors who performed the analyses and by the corresponding authors,[1] and in the instrument repositories at Aalto University and can be accessed upon request by contacting the corresponding author through the address present in the article notes. Access is also possible by contacting the responsible technicians of each of the instruments listed in the Experimental section of the article, at the Departments listed as notes a, b, and c of the article.

Supplementary information is available. See DOI: **https://doi.org/10.1039/d5ma00186b**

Acknowledgements

The authors acknowledge the provision of facilities by RawMatters Finland Infrastructure (RAMI, No. 292884), Aalto University Bioeconomy, OtaNano – Nanomicroscopy Center (Aalto-NMC), and the Micronova cleanroom facility of Aalto University. C. T., D. I. and I. T. acknowledges the Academy of Finland (projects 285972 and 319018) and C. T. thanks the

Vilho, Yriö ja Kalle Väisälä Foundation grant issued by the Finnish Academy of Sciences and Letters.

Notes and references

1 A. Fujishima and K. Honda, *Nature*, 1972, **238**, 37–38.
2 A. Fujishima, T. N. Rao and D. A. Tryk, *J. Photochem. Photobiol., C*, 2000, **1**, 1–21.
3 S. Bagheri, Z. A. Mohd Hir, A. T. Yousefi and S. B. Abdul Hamid, *Microporous Mesoporous Mater.*, 2015, **218**, 206–222.
4 H. Yao, M. Fan, Y. Wang, G. Luo and W. Fei, *J. Mater. Chem. A*, 2015, **3**, 17511–17524.
5 S. Jafari, B. Mahyad, H. Hashemzadeh, S. Janfaza, T. Gholikhani and L. Tayebi, *Int. J. Nanomed.*, 2020, **15**, 3447–3470.
6 X. Chen and S. S. Mao, *Chem. Rev.*, 2007, **107**, 2891–2959.
7 R. Daghrir, P. Drogui and D. Robert, *Ind. Eng. Chem. Res.*, 2013, **52**, 3581–3599.
8 J. Nowotny, *Energy Environ. Sci.*, 2008, **1**, 565–572.
9 U. Diebold, *Surf. Sci. Rep.*, 2003, **48**, 53–229.
10 F. A. Grant, *Rev. Mod. Phys.*, 1959, **31**, 646–674.
11 U. Diebold, *Appl. Phys. A: Mater. Sci. Process.*, 2003, **76**, 681–687.
12 T. Cao, T. Xia, L. Zhou, G. Li, X. Chen, H. Tian, J. Zhao, J.-O. Wang, W. Zhang, S. Li, S. Meng and H. Guo, *J. Phys. D: Appl. Phys.*, 2020, **53**, 424001.
13 T. Xia, Y. Zhang, J. Murowchick and X. Chen, *Catal. Today*, 2014, **225**, 2–9.
14 D. Kim, J. Hong, Y. R. Park and K. J. Kim, *J. Phys.: Condens. Matter*, 2009, **21**, 195405.
15 M. Parras, A. Varela, R. Cortés-Gil, K. Boulahya, A. Hernando and J. M. González-Calbet, *J. Phys. Chem. Lett.*, 2013, **4**, 2171–2176.
16 H. Peng, J. Li, S.-S. Li and J.-B. Xia, *Phys. Rev. B:Condens. Matter Mater. Phys.*, 2009, **79**, 092411.
17 A. Ajmal, I. Majeed, R. N. Malik, H. Idriss and M. A. Nadeem, *RSC Adv.*, 2014, **4**, 37003–37026.
18 X. Yan, T. Ohno, K. Nishijima, R. Abe and B. Ohtani, *Chem. Phys. Lett.*, 2006, **429**, 606–610.
19 F. R. Amalia, M. Takashima and B. Ohtani, *Chem. Commun.*, 2022, **58**, 11721–11724.
20 M. R. Abhilash, G. Akshatha and S. Srikantaswamy, *RSC Adv.*, 2019, **9**, 8557–8568.
21 C. N. C. Hitam and A. A. Jalil, *J. Environ. Manage.*, 2020, **258**, 110050.
22 M. S. S. Danish, L. L. Estrella, I. M. A. Alemaida, A. Lisin, N. Moiseev, M. Ahmadi, M. Nazari, M. Wali, H. Zaheb and T. Senjyu, *Metals*, 2021, **11**, 80.
23 D. Ihnatiuk, C. Tossi, I. Tittonen and O. Linnik, *Catalysts*, 2020, **10**, 1074.
24 D. Ihnatiuk, V. Vorobets, M. Šihor, C. Tossi, G. Kolbasov, N. Smirnova, I. Tittonen, A. Eremenko, K. Kocí and O. Linnik, *Appl. Nanosci.*, 2022, **12**, 565–577.
25 M. Sabharwal and M. Secanell, *Electrochim. Acta*, 2022, **419**, 140410.
26 J. Liang, Q. Liu, T. Li, Y. Luo, S. Lu, X. Shi, F. Zhang, A. M. Asiri and X. Sun, *Green Chem.*, 2021, **23**, 2834–2867.
27 A. M. Ahadi, O. Polonskyi, U. Schürmann, T. Strunskus and F. Faupel, *J. Phys. D: Appl. Phys.*, 2014, **48**, 035501.
28 S. Tanemura, L. Miao, W. Wunderlich, M. Tanemura, Y. Mori, S. Toh and K. Kaneko, *Sci. Technol. Adv. Mater.*, 2005, **6**, 11–17.
29 M. Malekzadeh and M. T. Swihart, *Chem. Soc. Rev.*, 2021, **50**, 7132–7249.
30 S. Ekeroth, E. P. Münger, R. Boyd, J. Ekspong, T. WÅgberg, L. Edman, N. Brenning and U. Helmersson, *Nano Lett.*, 2018, **18**, 3132–3137.
31 S. Ekeroth, J. Ekspong, D. K. Perivoliotis, S. Sharma, R. Boyd, N. Brenning, E. Gracia-Espino, L. Edman, U. Helmersson and T. WÅgberg, *ACS Appl. Nano Mater.*, 2021, **4**, 12957–12965.
32 S. Ekeroth, S. Ikeda, R. D. Boyd, T. Shimizu and U. Helmersson, *J. Nanopart. Res.*, 2019, **21**, 37.
33 C. Sudakar, P. Kharel, R. Suryanarayanan, J. S. Thakur, V. M. Naik, R. Naik and G. Lawes, *J. Magn. Magn. Mater.*, 2008, **320**, L31–L36.
34 A. Sarkar and G. G. Khan, *Nanoscale*, 2019, **11**, 3414–3444.
35 T. Mazza, E. Barborini, I. N. Kholmanov, P. Piseri, G. Bongiorno, S. Vinati, P. Milani, C. Ducati, D. Cattaneo, A. Li Bassi, C. E. Bottani, A. M. Taurino and P. Siciliano, *Appl. Phys. Lett.*, 2005, **87**, 103108.
36 M. Laitinen, M. Rossi, J. Julin and T. Sajavaara, *Nucl. Instrum. Methods Phys. Res., Sect. B*, 2014, **337**, 55–61.
37 K. Arstila, J. Julin, M. I. Laitinen, J. Aalto, T. Konu, S. Kärkkäinen, S. Rahkonen, M. Raunio, J. Itkonen, J. P. Santanen, T. Tuovinen and T. Sajavaara, *Nucl. Instrum. Methods Phys. Res., Sect. B*, 2014, **331**, 34–41.
38 S. Sainio, N. Wester, A. Aarva, C. J. Titus, D. Nordlund, E. I. Kauppinen, E. Leppänen, T. Palomäki, J. E. Koehne, O. Pitkänen, K. Kordas, M. Kim, H. Lipsanen, M. Mozetic, M. A. Caro, M. Meyyappan, J. Koskinen and T. Laurila, *J. Phys. Chem. C*, 2021, **125**, 973–988.
39 X. Wei, R. Skomski, B. Balamurugan, Z. G. Sun, S. Ducharme and D. J. Sellmyer, *J. Appl. Phys.*, 2009, **105**, 07C517.
40 T. H. Rana, P. Kumar, A. K. Solanki, R. Skomski and A. Kashyap, *J. Appl. Phys.*, 2013, **113**, 17B526.
41 J. Etula, K. Lahtinen, N. Wester, A. Iyer, K. Arstila, T. Sajavaara, T. Kallio, U. Helmersson and J. Koskinen, *Adv. Funct. Mater.*, 2019, **29**, 1904306.
42 C. J. Howard, T. M. Sabine and F. Dickson, *Acta Crystallogr., Sect. B: Struct. Sci.*, 1991, **47**, 462–468.
43 L. Dreesen, J.-F. Colomer, H. Limage, A. Giguère and S. Lucas, *Thin Solid Films*, 2009, **518**, 112–115.
44 H. Alizadeh, M. A. Mostaan, N. Malih and J. Davoodi, *Mol. Simul.*, 2020, **46**, 341–349.
45 D. R. Collins, W. Smith, N. M. Harrison and T. R. Forester, *J. Mater. Chem.*, 1996, **6**, 1385–1390.
46 P.-Q. Wang, Y. Bai, J.-Y. Liu, Z. Fan and Y.-Q. Hu, *Catal. Commun.*, 2012, **29**, 185–188.
47 Q.-Y. Liu, H.-D. Wang, R. Tang, Q. Cheng and Y.-J. Yuan, *ACS Appl. Nano Mater.*, 2021, **4**, 8674–8679.

48 L. Li, J. Yan, T. Wang, Z.-J. Zhao, J. Zhang, J. Gong and N. Guan, *Nat. Commun.*, 2015, **6**, 5881.
49 A. C. Ferrari and J. Robertson, *Phys. Rev. B:Condens. Matter Mater. Phys.*, 2001, **64**, 075414.
50 F. M. F. de Groot, M. Grioni, J. C. Fuggle, J. Ghijsen, G. A. Sawatzky and H. Petersen, *Phys. Rev. B:Condens. Matter Mater. Phys.*, 1989, **40**, 5715–5723.
51 J. G. Chen, *Surf. Sci. Rep.*, 1997, **30**, 1–152.
52 R. Brydson, H. Sauer, W. Engel, J. M. Thomass, E. Zeitler, N. Kosugi and H. Kuroda, *J. Phys.: Condens. Matter*, 1989, **1**, 797.
53 S. O. Kucheyev, T. van Buuren, T. F. Baumann, J. H. Satcher, T. M. Willey, R. W. Meulenberg, T. E. Felter, J. F. Poco, S. A. Gammon and L. J. Terminello, *Phys. Rev. B: Condens. Matter Mater. Phys.*, 2004, **69**, 245102.
54 V. S. Lusvardi, M. A. Barteau, J. G. Chen, J. Eng, B. Frühberger and A. Teplyakov, *Surf. Sci.*, 1998, **397**, 237–250.
55 L. X. Chen, T. Rajh, W. Jäger, J. Nedeljkovic and M. C. Thurnauer, *J. Synchrotron Radiat.*, 1999, **6**, 445–447.
56 R. Ruus, A. Kikas, A. Saar, A. Ausmees, E. Nõmmiste, J. Aarik, A. Aidla, T. Uustare and I. Martinson, *Solid State Commun.*, 1997, **104**, 199–203.
57 H. C. Choi, H.-J. Ahn, Y. M. Jung, M. K. Lee, H. J. Shin, S. B. Kim and Y.-E. Sung, *Appl. Spectrosc.*, 2004, **58**, 598–602.
58 P. Makula, M. Pacia and W. Macyk, *J. Phys. Chem. Lett.*, 2018, **9**, 6814–6817.
59 N. C. Diamantopoulos, A. Barnasas, C. S. Garoufalis, D. I. Anyfantis, N. Bouropoulos, P. Poulopoulos and S. Baskoutas, *Nanomaterials*, 2020, **10**, 2379.
60 T. Toyoda and I. Tsuboya, *Rev. Sci. Instrum.*, 2003, **74**, 782–784.
61 V. M. Naik, D. Haddad, R. Naik, J. Benci and G. W. Auner, *MRS Online Proc. Libr.*, 2003, **755**, 1112.
62 P. J. Wyatt, *Anal. Chem.*, 2014, **86**, 7171–7183.
63 J. Zhang, P. Liu, Z. Lu, G. Xu, X. Wang, L. Qian, H. Wang, E. Zhang, J. Xi and Z. Ji, *J. Alloys Compd.*, 2015, **632**, 133–139.
64 N. K. A. Hamed, M. K. Ahmad, N. H. H. Hairom, A. B. Faridah, M. H. Mamat, A. Mohamed, A. B. Suriani, C. F. Soon, F. I. M. Fazli, S. M. Mokhtar and M. Shimomura, *J. Sol-Gel Sci. Technol.*, 2022, **102**, 637–648.
65 J. Zhang, S. Yan, L. Fu, F. Wang, M. Yuan, G. Luo, Q. Xu, X. Wang and C. Li, *Chin. J. Catal.*, 2011, **32**, 983–991.
66 Q. V. Vo, L. T. T. Thao, T. D. Manh, M. V. Bay, B.-T. Truong-Le, N. T. Hoa and A. Mechler, *RSC Adv.*, 2024, **14**, 27265–27273.
67 H. Sudrajat and S. Babel, *Environ. Sci. Pollut. Res.*, 2016, 10177–10188.
68 Y. Nosaka and A. Y. Nosaka, *Chem. Rev.*, 2017, **117**, 11302–11336.
69 A. Turolla, A. Piazzoli, J. Farner Budarz, M. R. Wiesner and M. Antonelli, *Chem. Eng. J.*, 2015, **271**, 260–268.
70 B. Petrovicová, Z. Dahrouch, C. Triolo, F. Pantò, A. Malara, S. Patanè, M. Allegrini and S. Santangelo, *Appl. Sci.*, 2021, **11**, 9720.
71 S. M. Tichapondwa, J. P. Newman and O. Kubheka, *Phys. Chem. Earth*, 2020, **118–119**, 102900.
72 P. Subha and M. Jayaraj, *J. Exp. Nanosci.*, 2015, **10**, 1106–1115.